PCCP

PAPER

View Article Online
View Journal | View Issue

Cite this: *Phys. Chem. Chem. Phys.*, 2024, **26**, 2973

A bicomponent synergistic $Mo_xW_{1-x}S_2$/aluminum nitride vdW heterojunction for enhanced photocatalytic hydrogen evolution: a first principles study

Liang Xu,* [abd] Can Li,[a] S. X. Xiong,*[a] Shuaihao Tang,[a] Zhiqiang Xu,[b] Lei Cao,[a] Ji Tao,[a] Ying Zhang,[a] Kejun Dong *[c] and Ling-Ling Wang[d]

Received 7th November 2023,
Accepted 26th December 2023

DOI: 10.1039/d3cp05411j

rsc.li/pccp

The coupling of two-dimensional van der Waals heterojunctions is an effective way to achieve photocatalytic hydrogen production. This paper designs the $Mo_xW_{1-x}S_2$/AlN (x = 0, 0.25, 0.5, 0.75, 1) van der Waals heterojunction as a possible photocatalytic material. By using first-principles calculations, the effects of different Mo/W ratios on the band gap and photocatalytic hydrogen production performance of heterojunctions were investigated. The results show that the heterojunction is a direct Z-scheme photocatalyst and can achieve overall water splitting. By calculating the absorption spectrum, it is found that the heterojunction has a wider visible light absorption range when the bimetal is added, and there is still a strong absorption peak at 615 nm. With the increase of the Mo atom ratio, the absorption spectrum is red-shifted. The Gibbs free energy of the two-component $Mo_{0.5}W_{0.5}S_2$/AlN heterojunction is only −0.028 eV. Our work provides a new perspective for the modification of 2D transition metal dichalcogenide photocatalytic heterojunctions.

1 Introduction

Hydrogen is not only a common industrial raw material, but also an efficient, clean, and renewable secondary energy source.[1–5] According to the report on the future development trend of hydrogen energy published by the International Energy Agency (IEA), the consumption of hydrogen energy is expected to be 10 times the current consumption by 2050. Hydrogen energy is the key to the transformation of traditional energy sources. How to efficiently prepare hydrogen has become the main goal of current research. There are three main technologies for hydrogen production: water electrolysis hydrogen production[6,7] biomass hydrogen production[8,9] and solar hydrogen production.[10,11] The first method is often not cost-effective, while the second method is difficult to scale up due to the limitation of the biomass area.

In 1972, Fujishima and Honda of the University of Tokyo in Japan first reported photocatalytic water splitting to produce hydrogen on the TiO_2 single-crystal electrode, which opened the history of photocatalysis.[12] Recently, Dae-Hyeong Kim and Taeghwan Hyeon *et al.* from the Korea Institute of Basic Sciences designed a floating photocatalytic platform composed of porous elastomer–hydrogel nanocomposites, which has a high hydrogen evolution rate (up to 163 mmol h^{-1} m^{-2}). Under natural light, 79.2 ml of hydrogen can be produced per square meter per day by adding an economical single-atom Cu/TiO_2 photocatalyst. At the same time, it can also produce hydrogen stably and long-term in seawater and high turbidity water.[13] Previous studies have made photocatalytic hydrogen production a feasible solution.[14–17] The process of photocatalytic water splitting is roughly as follows: photocatalytic semiconductor absorbs photons to produce e^- and h^+, the photogenerated electrons transition to the conduction band, and a redox reaction occurs on the surface.[18–21] In theory, the more negative the conduction band potential is relative to the hydrogen electrode potential, the better the catalytic reduction ability of the material; the more positive the valence band potential is relative to the oxygen electrode potential, the better the oxidation performance of the material.[22–25] To decompose H_2O, the band edge position of the semiconductor needs to cross the water reduction potential (H^+/H_2) and the water oxidation potential (H_2O/O_2), so that the electrons and holes have enough energy to split the entire water.[26–30]

[a] *Nanchang Key Laboratory for Advanced Manufacturing of Electronic Information Materials and Devices, School of Energy and Mechanical Engineering, Jiangxi University of Science and Technology, Nanchang 330013, China. E-mail: liangxu@hnu.edu.cn, s.xiong@jxust.edu.cn*
[b] *Kungfu Sci-tech Co., Ltd., Nanchang 330096, China*
[c] *Centre for Infrastructure Engineering, School of Engineering, Design and Built Environment, Western Sydney University, Penrith, NSW 2751, Australia. E-mail: kejun.dong@westernsydney.edu.au*
[d] *Key Laboratory for Micro-Nano Optoelectronic Devices of Ministry of Education, School of Physics and Electronics, Hunan University, Changsha, 410082, China*

Two-dimensional TMDs (transition metal dichalcogenides) are a class of promising active photocatalysts. TMDs are usually denoted as MX_2 (M refers to transition metal elements; X refers to the elements of the VIA group).[31–34] The TMD monolayer contains three atomic layers, and the van der Waals force between the two adjacent layers is weak, so it is easy to peel off in the experiment. The advantages of TMDs as a photocatalyst are: (i) there are many active sites on the surface and edge of TMDs. (ii) Compared with traditional semiconductors, they have narrower band gaps to increase the light absorption range, improve solar energy utilization, and produce more photogenerated holes and electrons. (iii) Appropriate band positions to meet the thermodynamic requirements in the photocatalytic process. (iv) With the features of atomic thin layers, the short distance of carrier migration to the surface can prolong the lifetime of light quantum, and the large specific surface area is conducive to the capture of light, providing a good platform for doping and forming heterojunctions.[35–39]

The electronic band gap of TMDs can be tuned by changing the thickness of the material. It is found that when the bulk structure of TMDs is changed to the single-layer structure, the band gap increases from 0.88 eV to 1.71 eV, and the band structure is also changed. Other band gap control strategies are also under investigation.[40–42] In particular, $MoWS_2$ alloys with the chemical formula of $Mo_xW_{1-x}S_2$ were successfully crystallized in the 2H phase by chemical vapour transport (CVT) or flux zone growth.[43–46] As a potential photocatalyst material, the 2D aluminum nitride monolayer has strong energy stability, kinetic stability and thermal stability under water conditions. The monolayer is an indirect band gap semiconductor in the equilibrium state, and the band edge position is completely consistent with the redox potential of water. In addition, the monolayer has ultra-high ideal strength including flexibility and mechanical anisotropy superior to graphene. Previous studies on photocatalytic water splitting by MoS_2/AlN and the study of WS_2/AlN photocatalytic materials did not directly reflect the hydrogen evolution ability of the heterojunction.[47,48] Some of the previous studies on the hydrogen evolution performance of TMDs have used the ingenious strategy of orbital electron charging to effectively accelerate the desorption of OH_{ad}, thereby promoting the activity of alkaline photocatalytic hydrogen production.[49] Duoduo Gao *et al.* have focused on the influence and regulation of the transfer direction between the cocatalyst and the photocatalyst on the hydrogen adsorption energy of the active site.[50] We designed a series of $Mo_xW_{1-x}S_2$/AlN heterojunctions with different atomic ratios of Mo and W, and studied the change in the hydrogen evolution performance by adjusting the electronic structure of the material. It is concluded that the heterojunction under the synergistic effect of two components can promote hydrogen evolution.

In this paper, the electronic structure, optical properties and photocatalytic ability of direct Z-scheme $Mo_xW_{1-x}S_2$/AlN (x = 0, 0.25, 0.5, 0.75, 1) were systematically studied using density functional theory (DFT). In addition, various stability analyses confirmed the feasibility of the experimental preparation of the material. The calculation results show that the two types of heterostructures separate electrons and holes in space. Due to the transfer of charges, a built-in electric field from AlN to the $Mo_xW_{1-x}S_2$ electric field is formed. The energy band of $Mo_xW_{1-x}S_2$/AlN (x = 0, 0.25, 0.5, 0.75, 1) meets the requirements of photocatalytic water splitting. When bimetallic is added, the heterojunction exhibits better HER performance. In this work, the band gap and photocatalytic performance of the heterojunction were continuously adjusted by changing the proportion of metal atoms in TMDs, which provided a reasonable research idea and design direction for future experiments.

2 Computational methodology

Our density functional theory calculations are based on the VASP package.[51,52] For the $Mo_xW_{1-x}S_2$/AlN heterojunction, after convergence test and calculation, the electron wave function is expanded by the plane wave base group. During the calculation, the positions of all atoms are completely relaxed, and the energy convergence criterion and the atomic force convergence criterion are 10^{-6} eV and 0.01 eV Å^{-1}, respectively. We set the cutoff energy to 500 eV. A Monkhorst-centered 7 × 7 × 1 k-mesh was used for structural optimization and total energy calculations. To more accurately describe the vdW interaction between $Mo_xW_{1-x}S_2$ and the AlN layer, the vdW correction method DFT-D3 proposed by Grimme was used.[53–55] We set a 20 Å vacuum layer along the Z-axis to eliminate possible interactions between adjacent molecular layers. To obtain more accurate results, the energy band and optical absorption of all materials were calculated using the hybrid exchange–correlation functional HSE06.[56–58] Most of the data were processed using VASPKIT software.[59]

The binding energy, E_b, is calculated as:

$$E_b = E_{Mo_xW_{1-x}S_2/AlN} - E_{Mo_xW_{1-x}S_2} - E_{AlN} \quad (1)$$

where $E_{Mo_xW_{1-x}S_2/AlN}$ is the energy of the heterojunction, $E_{Mo_xW_{1-x}S_2}$ is the energy of $Mo_xW_{1-x}S_2$, and E_{AlN} is the energy of AlN.[60]

Young's modulus, Y, is calculated as:

$$Y = \frac{C_{11}^2 - C_{12}^2}{C_{11}} \quad (2)$$

where C_{11} and C_{12} represent two independent elastic constants, respectively.

The charge density difference is calculated as:

$$\Delta\rho = \rho_{Mo_xW_{1-x}S_2/AlN} - \rho_{Mo_xW_{1-x}} - \rho_{AlN} \quad (3)$$

where $\rho_{Mo_xW_{1-x}S_2/AlN}$, $\rho_{Mo_xW_{1-x}}$, and ρ_{AlN} represent the heterojunction and the charge density of each single layer, respectively.[61]

By calculating the hydrogen adsorption free energy of $Mo_xW_{1-x}S_2$/AlN (x = 0, 0.25, 0.5, 0.75, 1) at different Mo/W ratios, the hydrogen evolution ability of the active site can be obtained more directly. The Gibbs free energy ΔG is expressed as:

$$\Delta G = \Delta E_{abs} + \Delta E_{ZPE} - T\Delta S \quad (4)$$

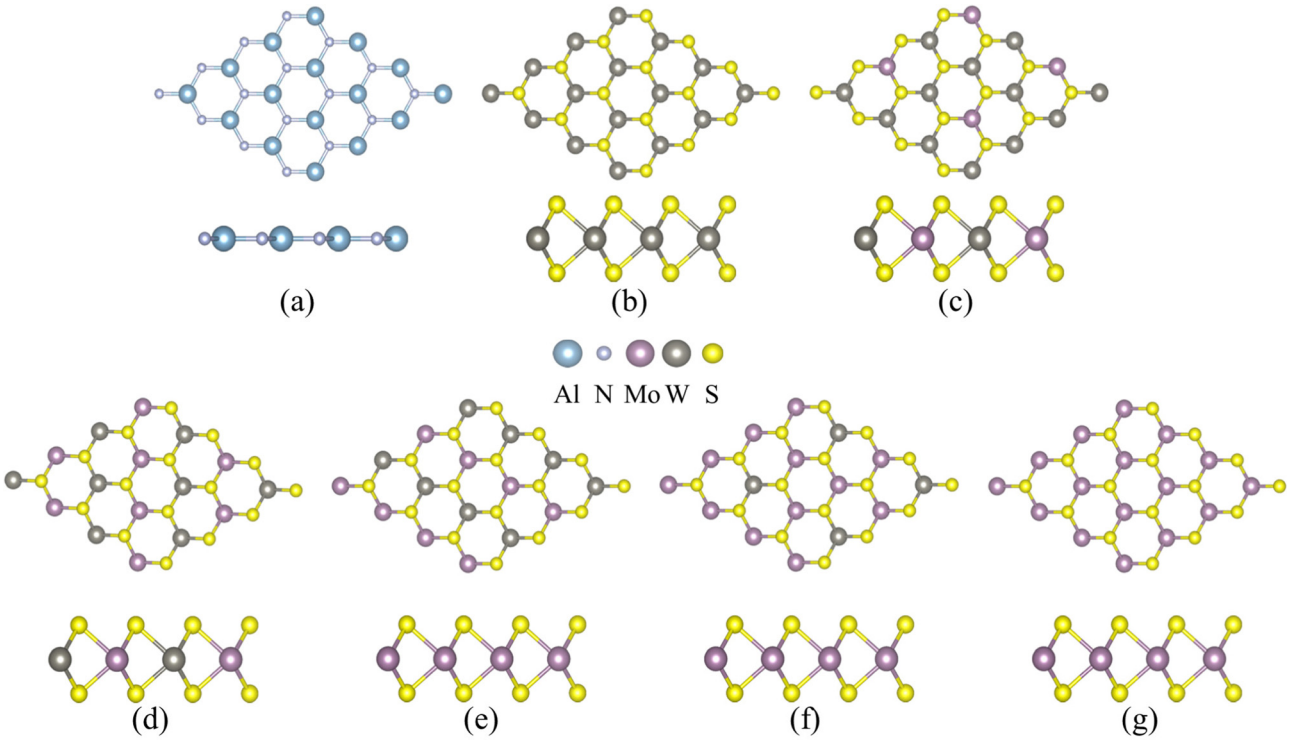

Fig. 1 Structures of (a) AlN, (b) WS_2, (c) $Mo_{0.25}W_{0.75}S_2$, (d) $Mo_{0.5}W_{0.5}S_2A$, (e) $Mo_{0.5}W_{0.5}S_2B$, (f) $Mo_{0.75}W_{0.25}S_2$, and (g) MoS_2 at different viewing angles.

where ΔG is the Gibbs free energy of the reaction in the intermediate process, and ΔE_{abs}, ΔE_{ZPE}, and ΔS represent the different adsorption energy of each intermediate reaction, respectively.[62]

3 Results and discussion

3.1 Various monolayer nanomaterials

We first designed $Mo_xW_{1-x}S_2$ (x = 0, 0.25, 0.5, 0.75, 1) independent molecular layers with different bimetallic ratios and the AlN independent molecular layer. As shown in Fig. 1, the $Mo_xW_{1-x}S_2$ monolayer structure is composed of three atomic layers, which is the same as the typical two-dimensional TMD configuration. When the ratio of Mo and W is 1 : 1, there are two atomic arrangement modes, named $Mo_{0.5}W_{0.5}S_2A$ and $Mo_{0.5}W_{0.5}S_2B$, respectively. The lattice constants of the optimized AlN, WS_2, and MoS_2 molecular layers are 3.122 Å, 3.181 Å, and 3.183 Å, respectively, which agree well with the previous calculation results.[63–65] To design $Mo_xW_{1-x}S_2$ molecular layers with different Mo/W atomic ratios, we performed a 2 × 2 × 1 supercell. The size of the supercell is shown in Table 1.

Table 1 The size of different monolayer 2 × 2 × 1 supercells, the size of the unit cell in the reference, the bond distance, the energy band size under different calculation methods and the comparison with the reference

System	a (Å)	b_{W-S} (Å)	b_{Mo-S} (Å)	E_g^{PBE} (eV)	E_g^{HSE06} (eV)
AlN	6.244/3.126[67]	Al–N 1.805	—	2.909	3.392/3.39[67]
WS_2	6.363/3.180[68]	2.416	—	1.816	2.017/2.06[68]
$Mo_{0.25}W_{0.75}S_2$	6.365	2.412	2.419	1.749	1.951
$Mo_{0.5}W_{0.5}S_2A$	6.366	2.415	2.414	1.704	1.908
$Mo_{0.5}W_{0.5}S_2B$	6.366	2.415	2.415	1.705	1.908
$Mo_{0.75}W_{0.25}S_2$	6.366	2.411	2.417	1.680	1.881
MoS_2	6.366/3.187[67]	—	2.413	1.673	1.866/1.92[67]

Then, we calculated the electronic structure of each independent molecular layer. The band and density of states of AlN, WS_2, and MoS_2 are shown in Fig. 2. The electronic structure information of $Mo_xW_{1-x}S_2$ under the bimetallic is shown in Fig. 3. It can be seen that the VBM and CBM of the AlN monolayer are located at different positions, showing an indirect band gap semiconductor; the VBM and CBM of $Mo_xW_{1-x}S_2$ monolayers are located at the same position in K space, showing a direct band gap semiconductor. By contrast, the electrons on the valence band of the direct bandgap semiconductor can be excited directly to the conduction band, avoiding the loss of energy in the phonon mode during the relaxation process, and the utilization of light is better. The band gaps of AlN, WS_2, and MoS_2 monolayers are 3.392 eV, 2.017 eV, and 1.866 eV, respectively, which are in good agreement with previous studies.[47,66]

From Table 1, it can be seen that the increase in the proportion of Mo atoms gradually reduces the band gap of the $Mo_xW_{1-x}S_2$ monolayer. It is worth noting that when the atomic ratio of Mo and W is 1 : 1, the band gaps obtained by different configurations are the same. In addition, according to the analysis of the density of states, the conduction band bottom and valence band top of the AlN monolayer are mainly provided by the p orbital of the N atom. The conduction band bottom and valence band top of monolayer MoS_2 are mainly

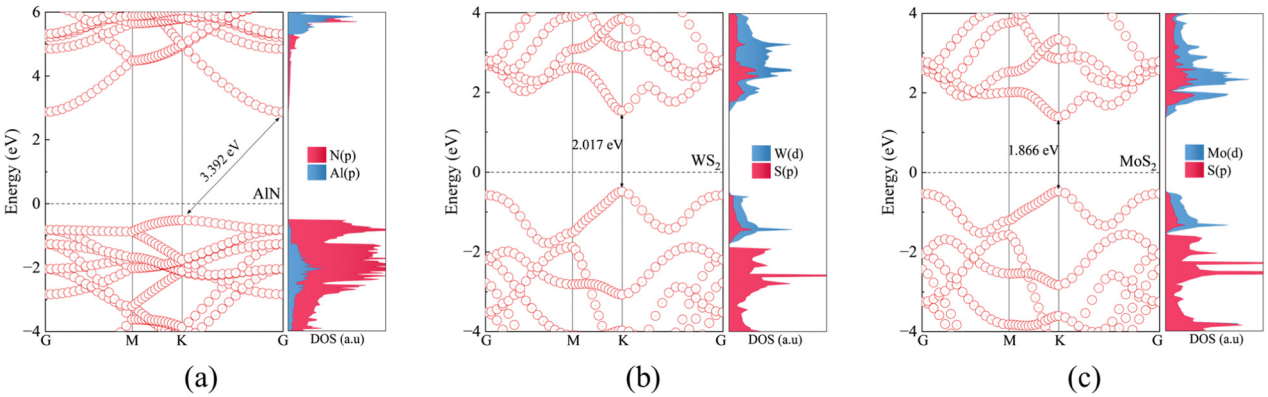

Fig. 2 The electronic structure of (a) AlN, (b) WS_2, and (c) MoS_2. The left and right sides correspond to the band and density of states calculated by the HSE06 method, respectively.

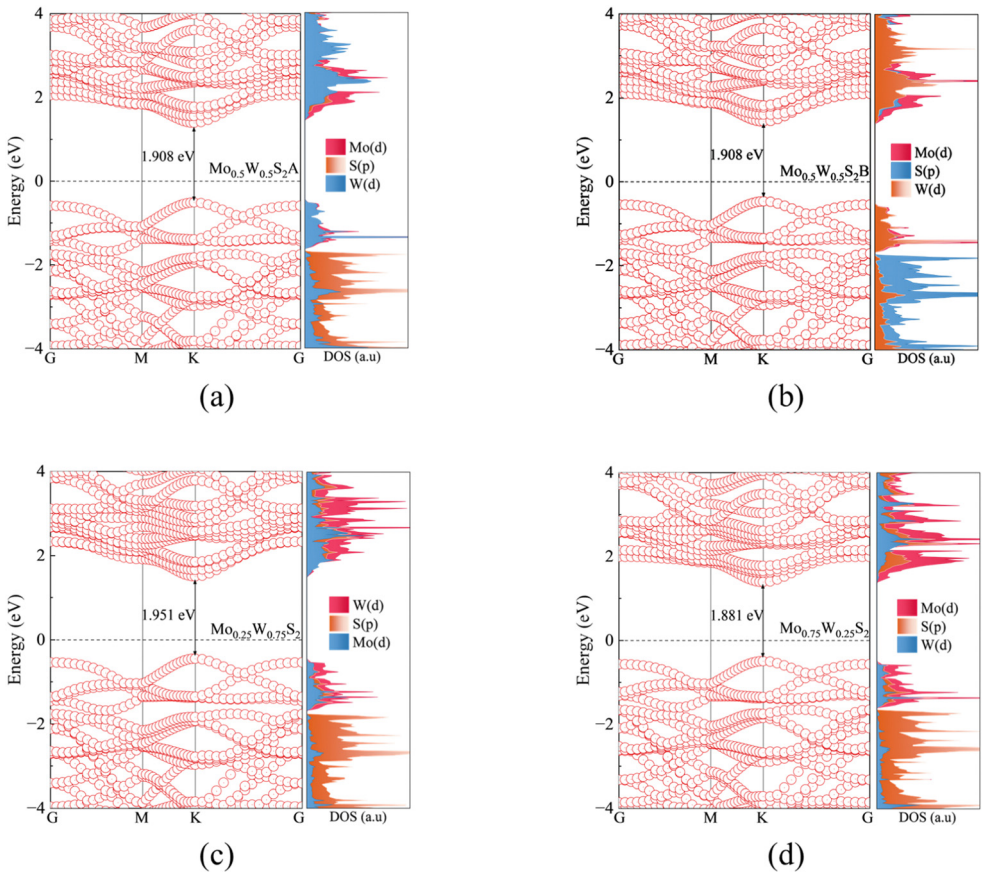

Fig. 3 The Electronic structure of (a) $Mo_{0.5}W_{0.5}S_2A$, (b) $Mo_{0.5}W_{0.5}S_2B$, (c) $Mo_{0.25}W_{0.75}S_2$, and (d) $Mo_{0.75}W_{0.25}S_2$. The left and right sides correspond to the band and density of states calculated by the HSE06 method, respectively.

contributed by the d orbital of Mo. The conduction band bottom and valence band top of the WS_2 monolayer are mainly occupied by the d orbital of the W atom.

3.2 Stability and electronic structure of composites

We take the first configuration ($Mo_{0.5}W_{0.5}S_2A$) and the AlN monolayer to construct a heterojunction, as an example, with its photocatalytic performance analyzed. The lattice mismatch of $Mo_{0.5}W_{0.5}S_2A$ and AlN is 1.9%, facilitating the stability of the van der Waals heterojunction. On this basis, six different stacking modes (such as Fig. 4) are studied. According to eqn (1), the binding energy E_b in different stacking modes is calculated. The results are shown in Table 2. It can be seen that these values are negative, indicating that these structures are stable. The interlayer binding energy in the van der Waals heterojunction is caused by the van der Waals force. The

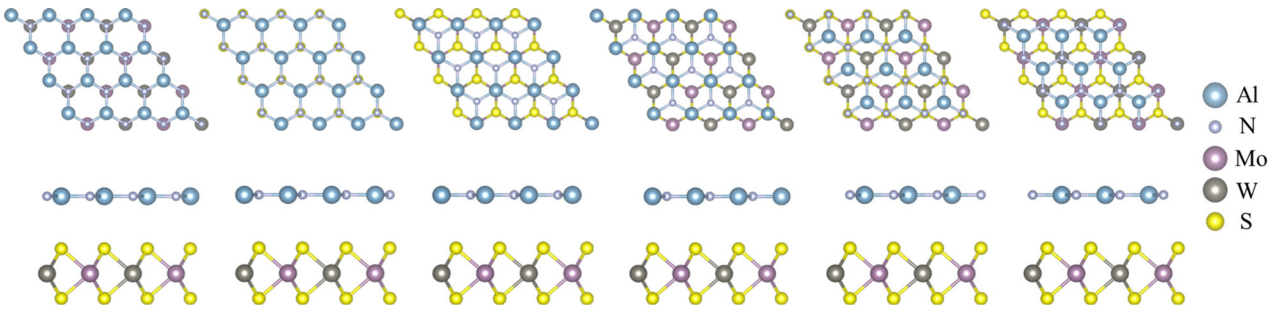

Fig. 4 $Mo_{0.5}W_{0.5}S_2A$/AlN heterojunction pattern in different stacking modes. The upper side is the top view and the lower side is the side view. From left to right, are the structures named Patter-A to Patter-F.

Table 2 The binding energy and layer distance for $Mo_{0.5}W_{0.5}S_2A$/AlN heterostructures in different stacking modes

	Stacking	E_b (eV)	h (Å)
AlN/$Mo_{0.5}W_{0.5}S_2A$	Pattern-A	−1.262	2.837
	Pattern-B	−0.672	3.498
	Pattern-C	−0.956	3.024
	Pattern-D	−1.276	2.777
	Pattern-E	−0.670	3.504
	Pattern-F	−0.960	3.042

arrangement of atoms will affect the distribution and strength of the van der Waals force, thus affecting the interlayer binding energy. Therefore, the binding energy is different in different stacking modes. The greater the negative value of the binding energy, the more stable the material structure. We choose the Pattern-D model as the standard model for the next calculation.

At room temperature T = 300 K, the motion of the molecular level system was simulated by Newtonian mechanics, and *ab initio* molecular dynamics (AIMD) was calculated to prove the thermal stability of the heterojunction. As shown in Fig. 5a, although the total potential energy of $Mo_{0.5}W_{0.5}S_2A$/AlN fluctuates, it can always reach the equilibrium value quickly within 5000 fs and then oscillates near the equilibrium value. The lattice vibration and dynamic stability of the crystal can be studied by the phonon spectrum, as shown in Fig. 5b. In the Brillouin zone, the distribution of all atoms at high and low frequencies is calculated to determine which atoms are easy to break away from the equilibrium position. No negative frequency is seen in all phonon branches, indicating that it has dynamic stability. The elastic constants of the structure are calculated to determine whether the structure has sufficient mechanical stability. For the $Mo_{0.5}W_{0.5}S_2A$/AlN structure, the two independent elastic constants are C_{11} = 276.353 N m^{-1}, and C_{12} = 84.607 N m^{-1}, respectively which satisfy $C_{11} > 0$, $C_{11} > |C_{12}|$, and the structure has good mechanical stability. With the above elastic constants, Young's modulus of the heterojunction is calculated as 250.450 N m^{-1} using eqn (2). The results show that the material is mechanically, kinetically and thermodynamically stable, which also confirms the feasibility of heterojunction synthesis in the experiment. Furthermore, the atomic bonding in the system can be determined by the electron localization function (ELF) shown in Fig. 5c. The upper layer is AlN and the lower layer is $Mo_{0.5}W_{0.5}S_2$. There is no equipotential line distribution in the dark blue region between the two layers, indicating that the force formed is the van der Waals force.

The electronic structure information of the $Mo_{0.5}W_{0.5}S_2A$/AlN van der Waals heterojunction is shown in Fig. 6. The red circle is the band of AlN, and the blue circle is the band of $Mo_{0.5}W_{0.5}S_2A$. It can be seen that the two band structures are interlaced. The VBM of the heterojunction is composed of AlN, and CBM is occupied by $Mo_{0.5}W_{0.5}S_2A$. The conduction band minimum and valence band maximum of the heterojunction

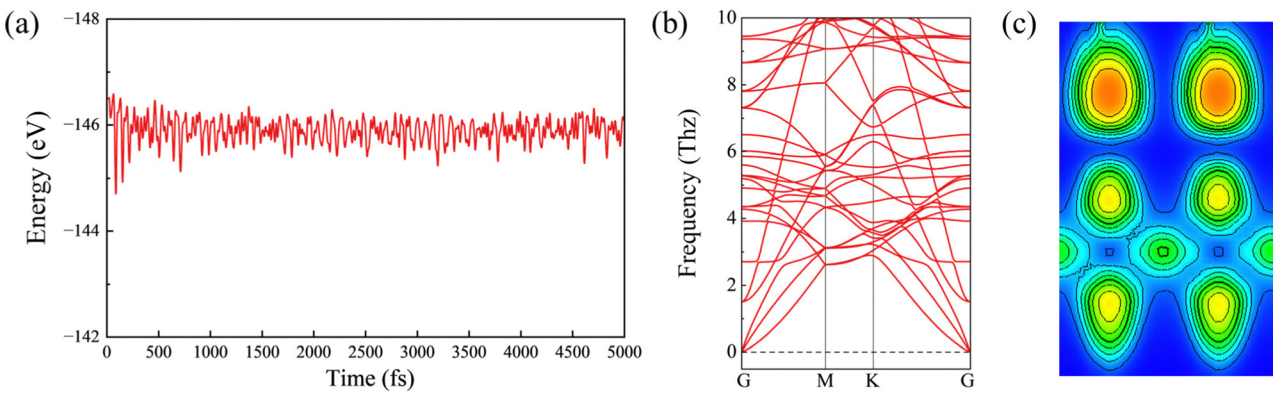

Fig. 5 $Mo_{0.5}W_{0.5}S_2A$/AlN heterojunction simulated by AIMD at T = 300 K: (a) total potential energy varies with time in 5000 fs and 1 fs as the time step; (b) the calculated phonon dispersion spectra of the heterojunction; and (c) an ELF of the heterojunction.

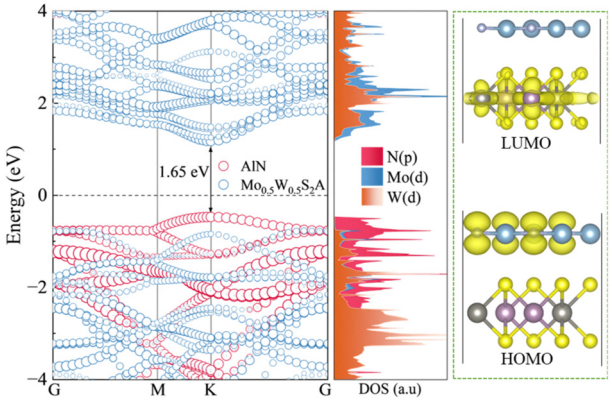

Fig. 6 The Electronic structure of the $Mo_{0.5}W_{0.5}S_2A$/AlN heterojunctions. Band structures and PDOS (left panel). The Fermi level is set to zero. HOMO and LUMO of heterojunction $Mo_{0.5}W_{0.5}S_2A$/AlN side view (right panel).

are located at the same position in *K* space. The band gap is 1.65 eV, showing a direct band gap type II orientation. According to the projected density of states, it can also be seen that VBM is occupied by the p orbital of the N atom, and CBM is provided by the d orbital of the Mo atom. It is also obvious that the highest occupied molecular orbital (HOMO) and the lowest unoccupied molecular orbital (LUMO) are contributed by two different components, which is consistent with the electronic structure information of the material.

3.3 Charge transfer and photocatalytic mechanism

The charge transfer mode is studied to determine whether the heterojunction is a conventional type-II or a direct Z-scheme heterojunction. The work function of a semiconductor is an important parameter that determines the charge redistribution and the formation of a built-in electric field when two layers of materials are combined. When two different monolayers form a heterojunction, the charge will flow between the layers until the Fermi level reaches equilibrium.[69–71] Therefore, we calculated the work function of AlN, $Mo_{0.5}W_{0.5}S_2A$ to analyze its charge transfer. The work function is defined as eqn (5) as follows:

$$\Phi = E_{vac} - E_f \quad (5)$$

where Φ is the work function, E_{vac} is the vacuum energy, and E_f is the Fermi level. The work function values of AlN and $Mo_{0.5}W_{0.5}S_2A$ are calculated to be 5.16 eV and 5.40 eV, respectively (Fig. 7). The work function of $Mo_{0.5}W_{0.5}S_2A$ is larger than that of AlN, indicating that the Fermi level of AlN is higher than that of $Mo_{0.5}W_{0.5}S_2A$. When two materials with different Fermi levels are combined, electrons flow from the conduction band of AlN to the conduction band of $Mo_{0.5}W_{0.5}S_2A$. The charge redistribution accumulation makes the AlN layer positively charged and the $Mo_xW_{1-x}S_2$ layer negatively charged, forming a built-in electrostatic field from AlN to $Mo_xW_{1-x}S_2$ at the interface. At the same time, a bending belt occurs. Under the action of the built-in electric field and the potential barrier formed by the band bending, the charge transfer along path-1 and path-2 is strongly inhibited (Fig. 8b), which enhances the combination of the photogenerated holes in the VB of the AlN layer and the photogenerated electrons in the CB of the $Mo_xW_{1-x}S_2$ layer (Path-3 in Fig. 8a). The photogenerated electrons of CB in AlN and the photogenerated holes of VB in $Mo_xW_{1-x}S_2$ participate in the reduction reaction and oxidation reaction respectively, which improves the photocatalytic performance. The calculation formula of the standard oxidation potential (O_2/H_2O) and the standard reduction potential (H^+/H_2) of water is:

$$E^{red}_{H^+/H_2} = -4.44\ eV + pH \times 0.059\ eV \quad (6)$$

$$E^{oxd}_{O_2/H_2O} = -5.67\ eV + pH \times 0.059\ eV \quad (7)$$

The band edge positions of Z-scheme AlN/$MoWS_2$ calculated by the HSE06 method are shown in Fig. 8a when pH is 0 and pH is 7. When the pH is 0–7, it crosses the redox potential of water, which proves its potential as a photocatalyst for total water splitting.

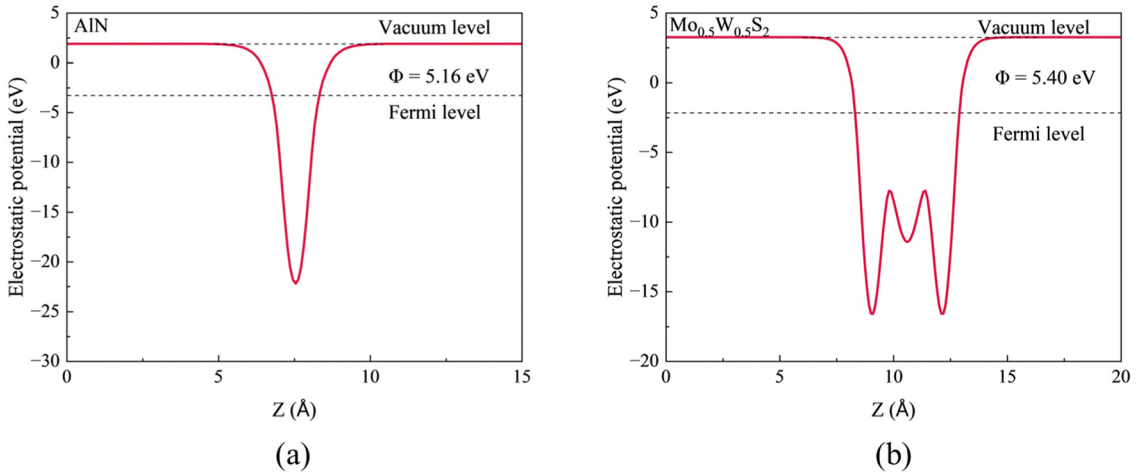

Fig. 7 Potential diagrams of AlN (a) and $Mo_{0.5}W_{0.5}S_2$ (b) monolayers. The imaginary line is used to reflect the vacuum level and the Fermi level respectively.

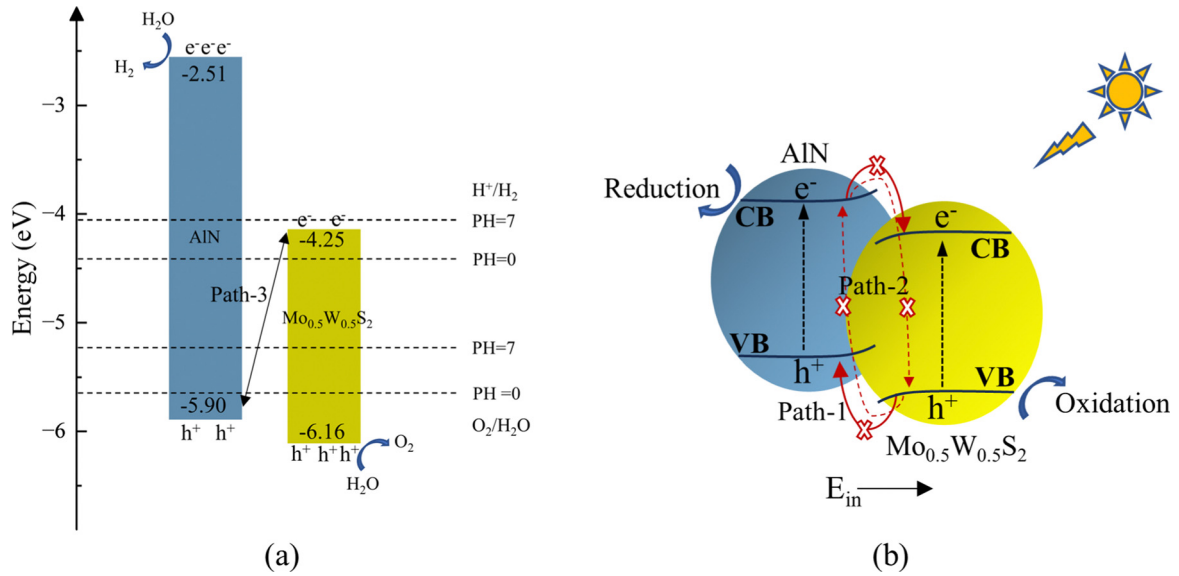

Fig. 8 (a) The relationship between the band edge position of $Mo_{0.5}W_{0.5}S_2$A/AlN heterojunction and the water redox potential at different pH values, (b) the water splitting mechanism of $Mo_{0.5}W_{0.5}S_2$A/AlN heterojunction under illumination.

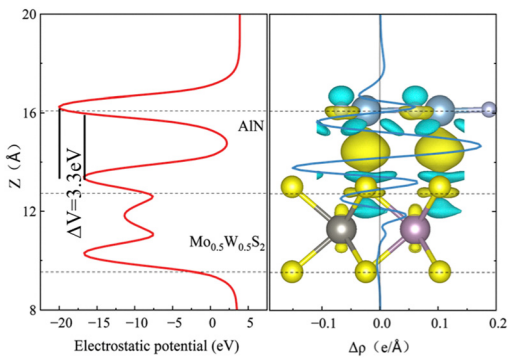

Fig. 9 The left is the electrostatic potential of the $Mo_{0.5}W_{0.5}S_2$A/AlN heterojunction, and the right is the three-dimensional charge density difference of the heterojunction with an isosurface value of $\rho = 7 \times 10^{-4}$ e Å. The electron accumulation part is yellow, and the electron depletion part is green, the blue line is the plane average charge density difference $\Delta\rho$ (Z). The positive $\Delta\rho$ represents the obtained electrons, and the negative $\Delta\rho$ represents the lost electrons.

Subsequently, we calculated the plane average charge density (using eqn (3)) and the three-dimensional charge density difference to further confirm this conclusion. The right side of Fig. 9 shows that the $Mo_{0.5}W_{0.5}S_2$A molecular layer (positive $\Delta\rho$) mainly obtains electrons, and the AlN molecular layer (negative $\Delta\rho$) mainly loses electrons. At the same time, it can be seen from the three-dimensional charge density difference diagram that the green part represents charge consumption and the yellow part represents charge accumulation that there is obvious charge transfer between the two monolayers of the heterojunction. The specific number of gain and loss electrons can be obtained by Bader charge analysis. The results show that when a heterojunction is formed, the number of electrons transferred from the AlN layer to the $Mo_{0.5}W_{0.5}S_2$A layer is 0.307. In the left part of Fig. 9, the potential drop (ΔV) between AlN and $Mo_{0.5}W_{0.5}S_2$A monolayer is 3.3 eV, which means that the built-in electric field is formed between the layers after electron transfer.

3.4 Electronic structures of heterojunctions with different Mo/W ratios

By changing the ratio of Mo and W atoms, the heterojunction band gap and photocatalytic performance can be continuously controlled. We calculated the electronic structure of the heterojunction at different Mo/W ratios. As shown in Fig. 10, for all $Mo_xW_{1-x}S_2$/AlN (x = 0, 0.25, 0.5, 0.75, 1) heterojunctions, the conduction and valence bands of AlN and $Mo_xW_{1-x}S_2$ (x = 0, 0.25, 0.5, 0.75, 1) are staggered. According to semiconductor physics, the minimum energy state in the conduction band and the highest energy state in the valence band are characterized by specific crystal momentum (k vector) in the Brillouin zone. In the monolayer, AlN is an indirect band gap semiconductor, and the $Mo_xW_{1-x}S_2$ (x = 0, 0.25, 0.5, 0.75, 1) monolayer is a direct band gap semiconductor. In the heterojunction formed by the two materials, AlN provides VBM, and $Mo_xW_{1-x}S_2$ monolayer provides CBM, which is at the same K point, indicating that AlN/$Mo_xW_{1-x}S_2$ (x = 0, 0.25, 0.5, 0.75, 1) is a direct band gap semiconductor. At the same time, since the crystal momentum of electrons and holes in the conduction band and valence band of the heterojunction is the same, an electron can directly emit a photon. According to the calculation of the density of states, the VBM of all heterojunctions are provided by N-p orbitals, the CBM of AlN/WS_2 are provided by W-d orbitals, and the CBM of the remaining heterojunctions are provided by Mo-d orbitals.

The calculated energy band of the x = 0 (WS_2/AlN) heterojunction is 1.82 eV, and the energy band of x = 1 (MoS_2/AlN) heterojunction is 1.59 eV, which is highly consistent with the previous literature.[47,48] The band gaps of $Mo_{0.25}W_{0.75}S_2$/AlN, $Mo_{0.5}W_{0.5}S_2$A/AlN, $Mo_{0.5}W_{0.5}S_2$B/AlN and $Mo_{0.75}W_{0.25}S_2$/AlN heterostructures are 1.72 eV, 1.65 eV, 1.65 eV and 1.6 eV,

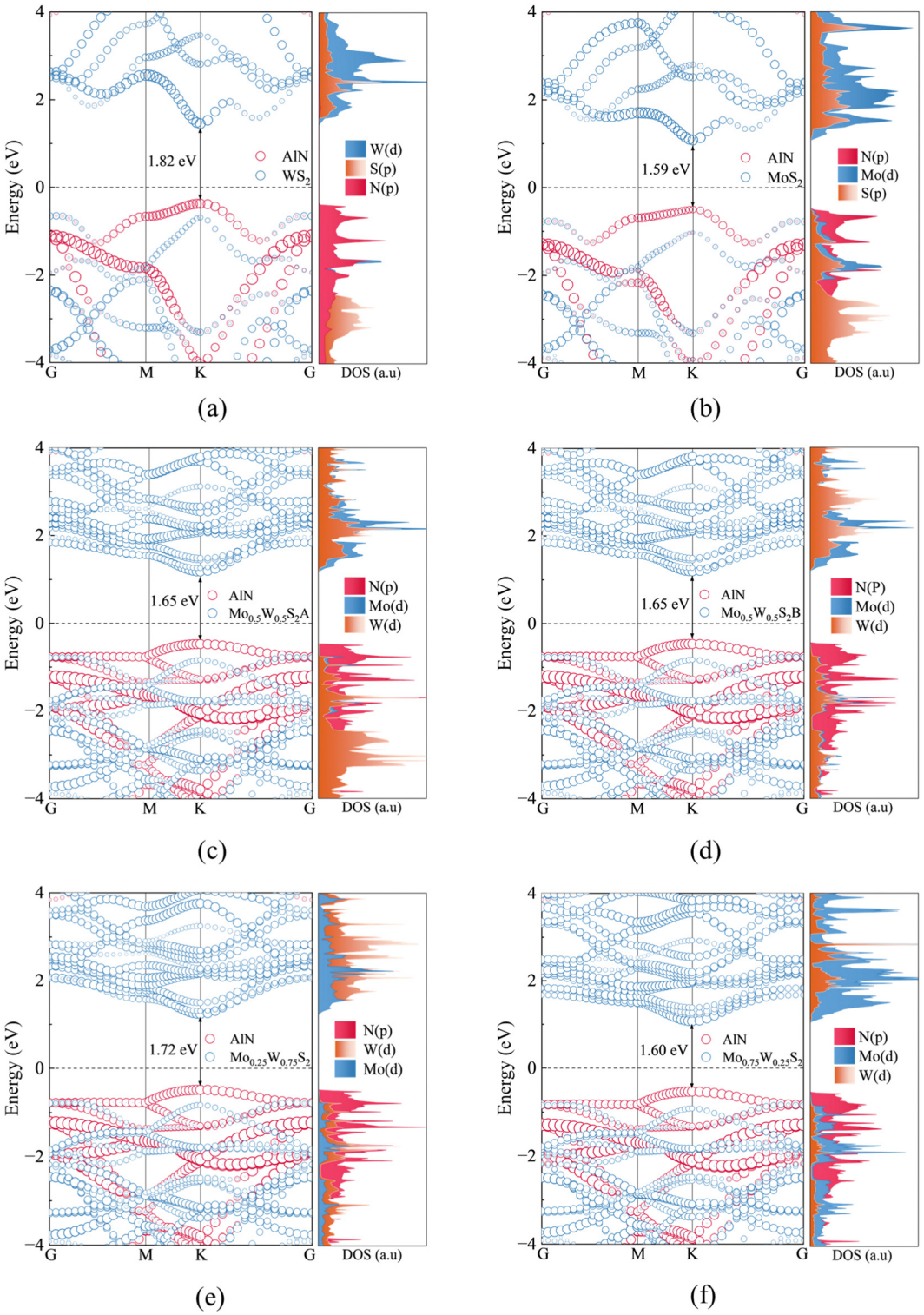

Fig. 10 The Electronic structure of (a) AlN/WS_2, (b) AlN/MoS_2, (c) AlN/$Mo_{0.5}W_{0.5}S_2$A, (d) AlN/$Mo_{0.5}W_{0.5}S_2$B, (e) AlN/$Mo_{0.25}W_{0.75}S_2$, (f) AlN/$Mo_{0.75}W_{0.25}S_2$. Band structures (left panel), PDOS (right panel).

respectively. Fig. 11 shows that as the ratio of Mo atoms increases, the band gap gradually decreases, and the charge transfer amount gradually increases from 0.26 electrons to 0.38 electrons. It can be seen that the band size is inversely proportional to the charge transfer amount. The band gap is relatively small, the energy required for the electron excitation transition is smaller and the charge exchange is increased. The band gap and charge exchange capacity of AlN/$Mo_{0.5}W_{0.5}S_2$ in two different configurations are not much different, the specific charge transfer amount of each atom in the heterojunction is shown in Table 3.

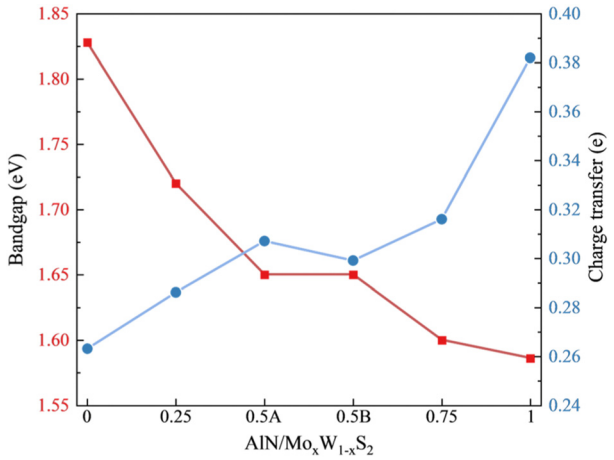

Fig. 11 The trend of band gap and charge transfer of heterojunction at different ratios of Mo and W atoms. The red line is the trend of the band gap of the heterojunction at different Mo/W ratios, the blue line represents the changing trend of heterojunction charge transfer under Bader calculation, and the lower axis is AlN/Mo$_x$W$_{1-x}$S$_2$ heterojunction at different X values.

3.5 Optical absorption

As a photolytic water material, the light absorption and utilization efficiency are very worthy of attention. To calculate the optical properties of Mo$_x$W$_{1-x}$S$_2$/AlN heterojunctions at different ratios, their frequency-dependent dielectric matrices were calculated using the Fermi golden rule under the dipole approximation.[72–75] The imaginary part $\varepsilon_2(\hbar\omega)$ of the dielectric function caused by the direct interband transition is given by the formula:

$$\varepsilon_2(\hbar\omega) = \frac{2e^2\pi}{\Omega\varepsilon_0}\sum_{k,v,c}\left|\langle\psi_k^c|u\cdot r|\psi_k^v\rangle\right|^2\delta\left(E_k^c - E_k^v - E\right) \quad (8)$$

ω represents the photon frequency, Ω represents the unit cell volume, u defines the polarization vector of the incident electric field, and v and c represent the valence band and the conduction band, respectively. The real part $\varepsilon_1(\omega)$ of the dielectric function is obtained by the Kramers–Kronig transformation of $\varepsilon_2(\omega)$. Then, the complex dielectric function is converted into the absorption coefficient α_{abs}, and the optical absorption spectrum is simulated according to the following relationship:

$$\alpha_{abs} = \sqrt{2}\omega\left(\sqrt{\varepsilon_1^2(\omega) + \varepsilon_2^2(\omega)} - \varepsilon_1(\omega)\right)^{1/2} \quad (9)$$

The imaginary part of the dielectric function and the absorption spectra of AlN, MoS_2 and WS_2 under the polarization vector perpendicular to the surface are shown in Fig. 12. The light absorption ability of the AlN monolayer is weak in the visible part, while the light absorption range of the MoS_2 monolayer is broader than that of WS_2, and there is still a strong absorption peak at 500 nm. Subsequently, we calculated the imaginary part of the dielectric function and the absorption spectrum of the Mo$_x$W$_{1-x}$S$_2$/AlN heterojunction with different ratios, confirming the light absorption ability of the heterojunction at various ratios. As shown in Fig. 13, the heterojunction can effectively absorb light in the

Table 3 Bader charge analysis of Mo$_x$W$_{1-x}$S$_2$/AlN (x = 0, 0.25, 0.5, 0.75, 1) heterojunctions. Positive values represent the gain of electrons, and negative values represent the loss of electrons

System\atom	W	Mo	S	Al	N	AlN	Mo$_x$W$_{1-x}$S$_2$	E_g (eV)
WS_2/AlN	−4.736	—	4.999	−9.164	8.901	−0.263	0.263	1.828
Mo$_{0.25}$W$_{0.75}$S$_2$/AlN	−3.548	−0.989	4.823	−9.163	8.877	−0.286	0.286	1.719
Mo$_{0.5}$W$_{0.5}$S$_2$A/AlN	−2.392	−2.025	4.724	−9.169	8.862	−0.307	0.307	1.648
Mo$_{0.5}$W$_{0.5}$S$_2$B/AlN	−2.316	−2.028	4.643	−9.167	8.868	−0.299	0.299	1.651
Mo$_{0.75}$W$_{0.25}$S$_2$/AlN	−1.194	−3.093	4.602	−9.167	8.852	−0.316	0.316	1.601
MoS_2/AlN	—	−4.070	4.452	−9.196	8.813	−0.382	0.382	1.586

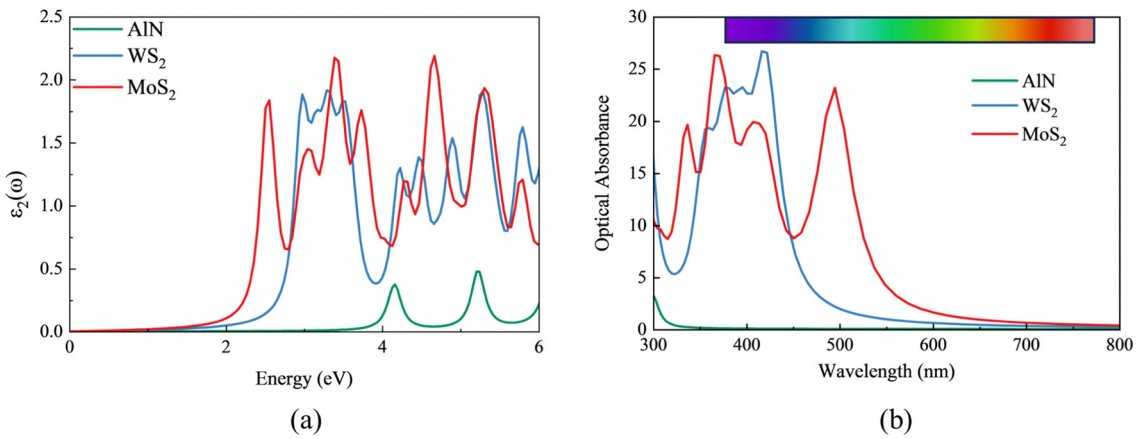

Fig. 12 (a) The imaginary part of the dielectric function of AlN, MoS_2 and WS_2 under the polarization vector perpendicular to the surface. (b) The absorption spectra of different monolayers, a wavelength range of 390–780 nm are visible light.

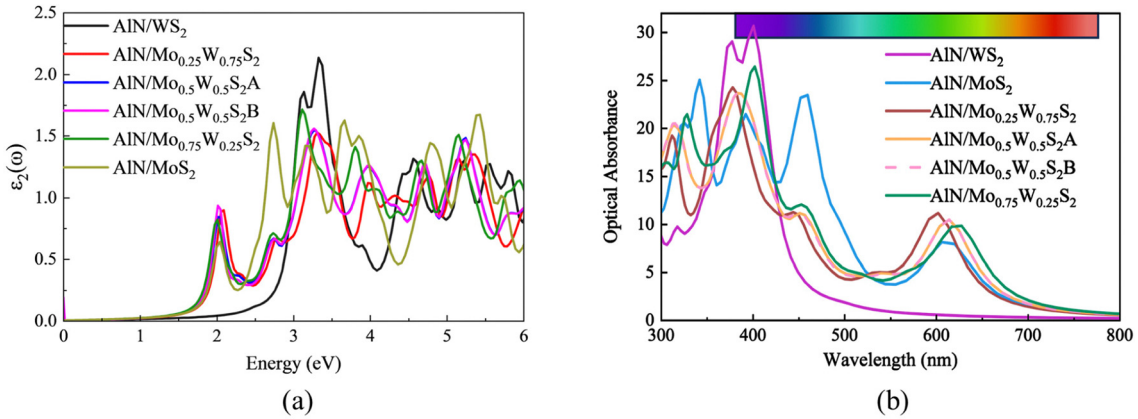

Fig. 13 (a) The imaginary part of the dielectric function of the heterojunctions with different Mo and W ratios under the polarization vector perpendicular to the surface. (b) The absorption spectra of the heterojunctions with different proportions, and the wavelength range of 390–780 nm is visible light.

visible range of ultraviolet and 390–650 nm. AlN/WS_2 only has a relatively high absorption peak at 400 nm, while AlN/MoS_2 can absorb visible light at 465 nm and 615 nm. It can be seen from the figure that with the addition of Mo atoms, an obvious absorption peak appears at about 615 nm, and with the increase of the Mo atomic ratio, the absorption spectrum appears redshifted. Compared with single-layer materials, the construction of $Mo_xW_{1-x}S_2$/AlN heterojunction greatly improves the light absorption range and solar utilization rate.

3.6 Hydrogen evolution reaction and oxygen evolution reaction

To study the hydrogen evolution ability of heterojunction more intuitively, we studied the photocatalytic HER performance of heterojunction at different ratios. The reaction mechanism of the HER is:

$$\begin{aligned} H^+ + e^- + * &\rightarrow H^* \\ H^* &\rightarrow \frac{1}{2}H_2 \end{aligned} \tag{10}$$

e^- denotes electron, H^+ denotes proton, * denotes catalyst, and H* denotes adsorbed H.

According to the simplified Norskov model proposed by J. K. Norskov, the first step $H^+ + e^- + * \rightarrow H^*$ is an energy-absorbing process, and the second step $H^* \rightarrow \frac{1}{2}H_2$ is an energy-releasing process. The free proton-electron pair reacts to obtain 1/2 H_2 of the product, and the mass and charge are conserved during the process. At PH = 0 and $U = 0$, the lower the energy of adsorption H and desorption H, the easier the reaction. Therefore, the hydrogen evolution ability is optimal when ΔG is close to 0.

According to eqn (4), we calculated the hydrogen evolution performance of monolayer AlN, WS_2, and MoS_2. As shown in Fig. 14(a), the ΔG of single-layer AlN, WS_2, and MoS_2 are 1.65 eV, 1.79 eV, and 1.60 eV, respectively. According to the principle of the HER, single-layer materials cannot effectively precipitate hydrogen. Then we calculated the HER performance of heterojunctions at different ratios. After testing, the active site of the HER of the AlN/$Mo_xW_{1-x}S_2$ heterojunction is the N atom. Compared with the single-layer material, the HER

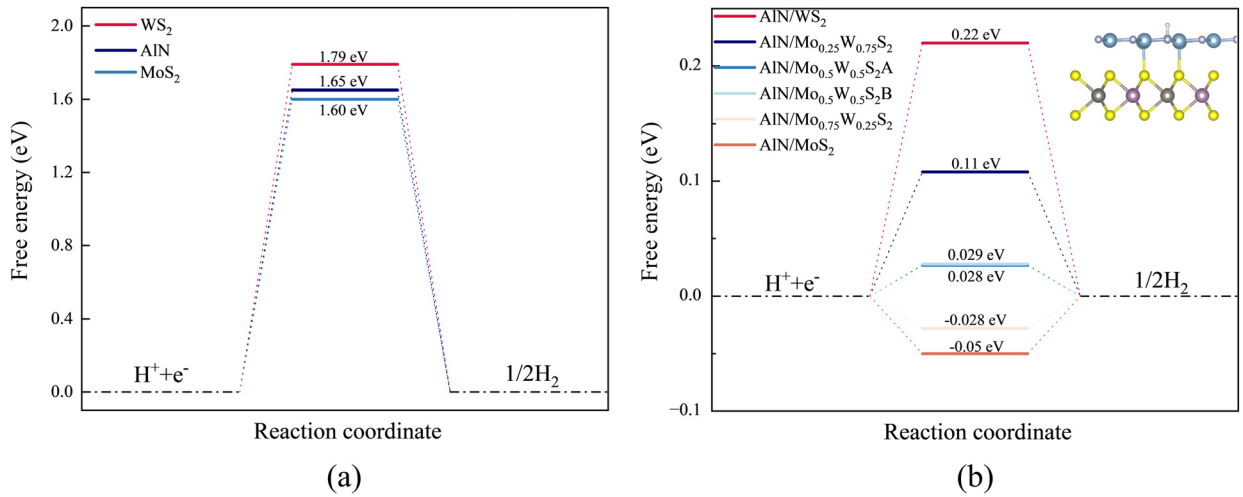

Fig. 14 (a) The free energy diagram of the HER on the monolayer AlN, WS_2, MoS_2 (T = 298.15 K). (b) The free energy diagram of the HER on the heterojunction at different ratios of Mo and W atoms (T = 298.15 K).

performance of the heterojunction has been significantly improved. Charge transfer and density of states (DOS) indicate that the heterojunction can rearrange the electron density, which is conducive to rapid charge/mass transfer. The charge transfer difference and hydrogen adsorption Gibbs free energy show that the heterojunction can adjust the electron cloud density and reduce the ΔG, thereby improving the catalytic activity. As shown in Fig. 14(b), it can be seen that the HER overpotential decreases first and then increases with the increase of the ratio of Mo atoms. Combined with the absorption spectra of heterojunctions at different Mo/W ratios, it is found that the HER performance of AlN/WS_2 is relatively poor, and its free energy ΔG = 0.22 eV. From the absorption spectra, it can be seen that AlN/WS_2 only has a strong absorption peak at 400 nm, and its visible light absorption range is smaller than other heterojunctions. When the ratio of Mo atom to W atom is 1 : 1 and 3 : 1, the visible light absorption range of the heterojunction is wider and the intensity is stronger, the adsorption energy of hydrogen is the smallest and closest to 0, and it is easier to precipitate hydrogen. Therefore, the heterojunction under the bimetallic achieves the best photocatalytic HER performance.

Since the AlN/$Mo_xW_{1-x}S_2$A heterojunction crosses the redox potential of water decomposition, we can test the heterojunction's oxygen evolution reaction (OER) at different Mo/W ratios. The energy difference between the two adjacent intermediate states is 1.23 eV when the OER occurs. However, in practice, the reaction requires an additional overpotential to make the reaction proceed smoothly.[76,77] The OER includes the following four steps:

$$* + H_2O = *OH + H^+ + e^- \quad (11)$$

$$*OH = *O + H^+ + e^- \quad (12)$$

$$*O + H_2O = *OOH + H^+ + e^- \quad (13)$$

$$*OOH = * + O_2 + H^+ + e^- \quad (14)$$

The rate of the OER is determined by the step with the largest increase in energy. Generally, the lower the energy of the rate-determining step is, the more likely the reaction is to occur. The Gibbs free energy ΔG_{OER} is expressed as:

$$\Delta G_{OER} = \Delta E_{ads} + \Delta E_{ZPE} - T\Delta S - eU \quad (15)$$

Among them, ΔE_{ads}, ΔE_{ZPE} are the adsorption energy difference of the intermediate reaction, T is the temperature of 298.15 K, ΔS is the entropy energy change calculated by frequency, and eU is the energy added to the free energy at each step when the reference standard hydrogen electrode is used. The overpotential of the OER is calculated as:

$$U^{OER} = \frac{\max\{\Delta G\}}{e} - 1.23 \quad (16)$$

The active site of the OER of the AlN/$Mo_xW_{1-x}S_2$ heterojunction is the S atom. It can be seen from Fig. 15 that with the increase of Mo atoms, the overpotential of AlN/$Mo_xW_{1-x}S_2$ (x = 0, 0.25, 0.5, 0.75, 1) heterojunctions shows a downward trend, and the minimum value is obtained when the Mo/W ratio is 3 : 1. The

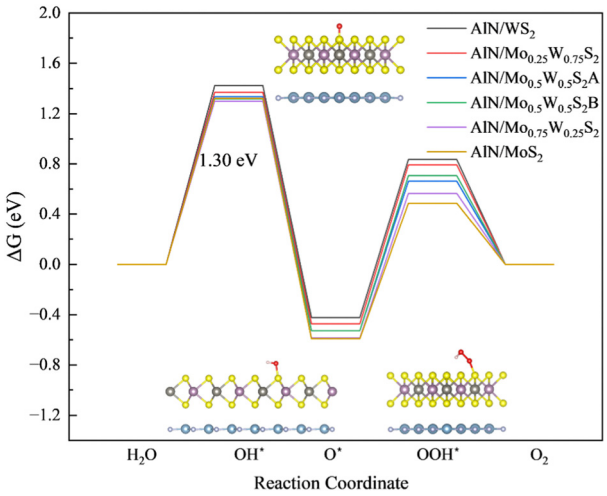

Fig. 15 The Gibbs free energy change diagram of the OER of AlN/$Mo_xW_{1-x}S_2$ heterojunctions with different Mo/W ratios. (T = 298.15 K).

overpotentials of AlN/WS_2, AlN/$Mo_{0.25}W_{0.75}S_2$, AlN/$Mo_{0.5}W_{0.5}S_2$A, AlN/$Mo_{0.5}W_{0.5}S_2$B, AlN/$Mo_{0.75}W_{0.25}S_2$ and AlN/MoS_2 are 1.422 eV, 1.371 eV, 1.335 eV, 1.319 eV, 1.300 eV and 1.323 eV, respectively. This is lower than the overpotential of the previously studied GaN/$Mg(OH)_2$ heterojunction (1.68 eV)[78] and is close to the OER performance of commercial photocatalyst TiO_2 (>1 eV).[79] These results indicate that AlN/$Mo_xW_{1-x}S_2$ can be used as a potential photocatalytic material to achieve full water splitting. The change of the two-component ratio also provides a direction for the design and research of the heterojunction.

In summary, the photocatalytic properties of $Mo_xW_{1-x}S_2$/AlN heterojunction with different metal ratios were calculated by first principles. These characteristics indicate that the heterojunction is beneficial to the separation of photogenerated electrons and holes, and has the potential to be applied to photocatalytic reactions.

4 Conclusion

In this paper, the photocatalytic properties of $Mo_xW_{1-x}S_2$/AlN (x = 0, 0.25, 0.5, 0.75, 1) van der Waals heterojunctions were systematically studied. The results show that these heterojunctions as direct Z-scheme photocatalysts satisfy the condition of complete water splitting. The separation of photogenerated electrons and holes on different material layers greatly improves the photocatalytic efficiency. Through further analysis of the electronic structure, we found that with the increase of the Mo atom ratio, the band gap of $Mo_xW_{1-x}S_2$/AlN (x = 0, 0.25, 0.5, 0.75, 1) gradually decreases, and the charge exchange ability increases. The calculation results of the HER free energy show that when bimetallic is added, the heterojunction has the advantage of a high light absorption range and exhibits the best photocatalytic HER performance. Our research realizes the continuous regulation of the electronic structure and hydrogen evolution performance of the heterojunction by adjusting the proportion of metal atoms in the TMD heterojunction. The

research results provide a new strategy for the regulation and modification of TMDs and other two-dimensional heterojunction materials.

Conflicts of interest

The authors declare no competing financial interest.

Acknowledgements

This work was financially supported by the National Nature Science Foundation of China (Grant No. 52263031) and the Jiangxi Provincial Natural Science Foundation (Grant No. 20212BAB201013 and 20202ACBL211004).

Notes and references

1 A. Ahmed, A. Q. Al-Amin, A. F. Ambrose and R. Saidur, *Int. J. Hydrogen Energy*, 2016, **41**, 1369–1380.
2 J. Bae, S. Lee, S. Kim, J. Oh, S. Choi, M. Bae, I. Kang and S. P. Katikaneni, *Int. J. Hydrogen Energy*, 2016, **41**, 19990–20022.
3 N. Hacking, P. Pearson and M. Eames, *Int. J. Hydrogen Energy*, 2019, **44**, 29805–29848.
4 M. Liu, Z. Yao, J. Gu, C. Li, X. Huang, L. Zhang, Z. Huang and M. Fan, *Chem. Eng. J.*, 2023, **461**, 141918.
5 A. Zubaryeva and C. Thiel, *Int. J. Hydrogen Energy*, 2013, **38**, 15878–15886.
6 N. Bidin, S. R. Azni, M. A. Abu Bakar, A. R. Johari, D. H. F. Abdul Munap, M. F. Salebi, S. N. Abd Razak, N. S. Sahidan and S. N. A. Sulaiman, *Int. J. Hydrogen Energy*, 2017, **42**, 133–142.
7 C. Lamy, *Int. J. Hydrogen Energy*, 2016, **41**, 15415–15425.
8 C.-C. Cormos, *Energy*, 2023, **270**, 126926.
9 H. Gu, S. Lang, G. Song, S. Zhang, M. Niu, W. Liu and L. Shen, *Chem. Eng. J.*, 2019, **360**, 260–270.
10 M. K. Abbas, Q. Hassan, V. S. Tabar, S. Tohidi, M. Jaszczur, I. S. Abdulrahman and H. M. Salman, *Int. J. Hydrogen Energy*, 2023, **48**, 2929–2948.
11 B. Geng, B. Guene Lougou, Y. Shuai, H. Zhang, Q. Pan, D. Han, B. Jiang, L. Wu and Z. Wang, *Renewable Sustainable Energy Rev.*, 2023, **175**, 113169.
12 A. Fujishima and K. Honda, *Nature*, 1972, **238**, 37–38.
13 C. W. L. Wang Hee Lee, G. D. Cha, B.-H. Lee, J. H. Jeong, H. Park, J. Heo, M. S. Bootharaju, S.-H. Sunwoo, J. H. Kim, K. H. Ahn, D.-H. Kim and T. Hyeon, *Nat. Nanotechnol.*, 2023, **18**, 754–762.
14 M. Gar Alalm, A. Tawfik and S. Ookawara, *J. Water Process Eng.*, 2015, **8**, 55–63.
15 S. Tang, L. Xu, K. Dong, Q. Wang, J. Zeng, X. Huang, H. Li, L. Xia and L. Wang, *Appl. Surf. Sci.*, 2023, **615**, 156357.
16 L. Xu, J. Tao, B. Xiao, F. Xiong, Z. Ma, J. Zeng, X. Huang, S. Tang and L.-L. Wang, *Phys. Chem. Chem. Phys*, 2023, **25**, 3969–3978.
17 S. Tang, L. Xu, B. Peng, F. Xiong, T. Chen, X. Luo, X. Huang, H. Li, J. Zeng, Z. Ma and L.-L. Wang, *Appl. Surf. Sci.*, 2022, **575**, 151655.
18 G. Nagaraju, T. N. Ravishankar, K. Manjunatha, S. Sarkar, H. Nagabhushana, R. Goncalves and J. Dupont, *Mater. Lett.*, 2013, **109**, 27–30.
19 L.-B. Zhan, C.-L. Yang, M.-S. Wang and X.-G. Ma, *Appl. Surf. Sci.*, 2023, **626**, 157215.
20 Y. Zhao, B. Zhang and J. Lin, *Appl. Surf. Sci.*, 2023, **621**, 156883.
21 H. Li, L. Xu, X. Huang, J. Ou-Yang, M. Chen, Y. Zhang, S. Tang, K. Dong and L.-L. Wang, *Int. J. Hydrogen Energy*, 2023, **48**, 2186–2199.
22 X.-J. Lv, S. Zhou, X. Huang, C. Wang and W.-F. Fu, *Appl. Catal., B*, 2016, **182**, 220–228.
23 L. Li, T. Huang, K. Liang, Y. Si, J.-C. Lian, W.-Q. Huang, W. Hu and G.-F. Huang, *Phys. Rev. Applied*, 2022, **18**, 014013.
24 D. W. R. He, N. Luo, J. Zeng, K.-Q. Chen and L.-M. Tang, *Phys. Rev. Lett*, 2023, **130**, 046401.
25 J. Zeng, L. Xu, X. Luo, T. Chen, S.-H. Tang, X. Huang and L.-L. Wang, *Tungsten*, 2022, **4**, 52–59.
26 H. Chen, C. Tan, K. Zhang, W. Zhao, X. Tian and Y. Huang, *Appl. Surf. Sci.*, 2019, **481**, 1064–1071.
27 N. Fajrina and M. Tahir, *Int. J. Hydrogen Energy*, 2019, **44**, 540–577.
28 H. Sepahvand and S. Sharifnia, *Int. J. Hydrogen Energy*, 2019, **44**, 23658–23668.
29 G. Hou, X. Jia, H. Kang, X. Qiao, Y. Liu, Y. Li, X. Wu and W. Qin, *Appl. Catal., B*, 2022, **315**, 121551.
30 G. Liu, T. Chen, G. Zhou, Z. Xu and X. Xiao, *ACS Sens*, 2023, **8**, 1440–1449.
31 J. Radhakrishnan, S. Ratna and K. Biswas, *Inorg. Chem. Commun.*, 2022, **145**, 109971.
32 L. Wang, D. Liu, L. Jiang, Y. Ma, G. Yang, Y. Qian and W. Lei, *Nano Energy*, 2022, **98**, 107192.
33 X. Dong, T. Chen, G. Liu, L. Xie, G. Zhou and M. Long, *ACS Sens*, 2022, **7**, 3450–3460.
34 S. Tang, L. Xu, K. Dong, Q. Wang, J. Zeng, X. Huang, H. Li, L. Xia and L. Wang, *Appl. Surf. Sci.*, 2023, **615**, 156357.
35 B. Anandha Priya, T. Sivakumar and P. Venkateswari, *Inorg. Chem. Commun.*, 2022, **136**, 109118.
36 H. Liu, L. Xu, Z. Ma, Z. Li, Y. Zhang, B. Zhang and L.-L. Wang, *Mater. Today Commun.*, 2023, **36**, 106578.
37 G. Yongxin and D. Yunxi, *Chem. Phys. Lett.*, 2022, **803**, 139828.
38 X. Zhan, H. Hou, D. Ou, H. Zhang, B. Li, L. Jiang, F. Gao, L. Xu and W. Yang, *Mater. Today Energy*, 2023, 101311.
39 M. Ma, H. Yu, L. Deng, L. Wang, S. Liu, H. Pan, J. Ren, M. Y. Maximov, F. Hu and S. Peng, *Tungsten*, 2023, **5**, 589–597.
40 S. Joseph, J. Mohan, S. Lakshmy, S. Thomas, B. Chakraborty, S. Thomas and N. Kalarikkal, *Mater. Chem. Phys.*, 2023, **297**, 127332.
41 I. J. Mphahlele, S. P. Malinga and L. N. Dlamini, *Sustainable Chem. Pharm.*, 2021, **24**, 100549.
42 L. Xu, Q. Zeng, S. Xiong, Y. Zhang, L. Cao, J. Tao, Z. Li, L.-L. Wang and K. Dong, *Int. J. Hydrogen Energy*, 2024, **50**, 352–364.
43 D. Gao, B. Zhao, L. Wang, E. Aslan, I. Hatay Patir, J. Yu and H. Yu, *Chem. Eng. J.*, 2022, **449**, 137803.
44 A. Kokliukhin, M. Nikulshina, A. Mozhaev, C. Lancelot, C. Lamonier, N. Nuns, P. Blanchard, A. Bugaev and P. Nikulshin, *Catal. Today*, 2021, **377**, 26–37.

45 W. Li, F. Li, Y. Liu, J. Li, H. Huo and R. Li, *Int. J. Hydrogen Energy*, 2017, **42**, 18774–18784.
46 B. Sun, S. Yang, Y. Guo, Y. Xue, J. Tian, H. Cui and X. Song, *J. Colloid Interface Sci.*, 2019, **547**, 339–349.
47 J. Liao, B. Sa, J. Zhou, R. Ahuja and Z. Sun, *J. Phys. Chem. C.*, 2014, **118**, 17594–17599.
48 C. Attaccalite, M. S. Prete and M. Palummo, *Materials*, 2022, **15**(23), 8318.
49 W. Zhong, J. Xu, X. Zhang, J. Zhang, X. Wang and H. Yu, *Adv. Funct. Mater.*, 2023, **33**, 2302325.
50 D. Gao, P. Deng, J. Zhang, L. Zhang, X. Wang, H. Yu and J. Yu, *Angew. Chem., Int. Ed.*, 2023, e202304559.
51 R. Bodlos, V. Fotopoulos, J. Spitaler, A. L. Shluger and L. Romaner, *Materialia*, 2022, **21**, 101362.
52 M. Jiang, H. Du, A. Gan, M. Ni and B. Zhao, *J. Nucl. Mater.*, 2023, **581**, 154452.
53 K. Boezar, A. Reisi-Vanani and M. Dehkhodaei, *Int. J. Hydrogen Energy*, 2021, **46**, 38370–38380.
54 T. Condon-Baxendale, N. Ploysongsri, M. Petchmark and V. Ruangpornvisuti, *Vacuum*, 2023, **209**, 111798.
55 B. Kaewruksa, A. Du and V. Ruangpornvisuti, *Int. J. Hydrogen Energy*, 2022, **47**, 29896–29906.
56 B. J. Abdullah, *Mater. Sci. Semicond. Process.*, 2022, **137**, 106214.
57 M. Irfan, S. Azam, Z. Abbas and S. Goumri-Said, *Optik*, 2022, **262**, 169297.
58 J. Tao, L. Xu, C. Li, S. Xiong, Z. Xu, J. Shao, L. Cao, Y. Zhang, K. Dong and L.-L. Wang, *Phys. Chem. Chem. Phys*, 2023, **25**, 30924–30933.
59 V. Wang, N. Xu, J.-C. Liu, G. Tang and W.-T. Geng, *Comput. Phys. Commun.*, 2021, **267**, 108033.
60 Z. Ma, L. Xu, K. Dong, T. Chen, S. X. Xiong, B. Peng, J. Zeng, S. Tang, H. Li, X. Huang, K.-W. Luo and L.-L. Wang, *Int. J. Hydrogen Energy*, 2022, **47**, 7202–7213.
61 L. Xu, Y. Zhang, Z. Ma, T. Chen, C. Guo, C. Wu, H. Li, X. Huang, S. Tang and L.-L. Wang, *Int. J. Hydrogen Energy*, 2023, **48**, 18301–18314.
62 C. Zhang, Y. Yuan, B. Jia, F. Wei, X. Zhang, G. Wu, L. Li, C. Chen, Z. Zhao, F. Chen, J. Hao and P. Lu, *Appl. Surf. Sci.*, 2023, **622**, 156894.
63 D. Gupta, V. Chauhan and R. Kumar, *Inorg. Chem. Commun.*, 2020, **121**, 108200.
64 J. He, X. Wei, Y. Jia, J. Liu, Y. Tian, Y. Zhang, J. Fan, T. Guo, L. Ni and L. Duan, *Phys. E*, 2021, **132**, 114754.
65 L. Ju, Y. Dai, W. Wei, M. Li and B. Huang, *Appl. Surf. Sci.*, 2018, **434**, 365–374.
66 G. Wang, S. Dang, P. Zhang, S. Xiao, C. Wang and M. Zhong, *J. Phys. D*, 2018, **51**, 025109.
67 J. Liao, B. Sa, J. Zhou, R. Ahuja and Z. Sun, *J. Phys. Chem. C*, 2014, **118**, 17594–17599.
68 G. Wang, S. Dang, P. Zhang, S. Xiao, C. Wang and M. Zhong, *J. Phys. D: Appl. Phys.*, 2017, **51**, 025109.
69 S. Sk, C. S. Vennapoosa, A. Tiwari, B. M. Abraham, M. Ahmadipour and U. Pal, *Int. J. Hydrogen Energy*, 2022, **47**, 33955–33965.
70 C. S. Vennapoosa, S. Varangane, B. M. Abraham, V. Perupogu, S. Bojja and U. Pal, *Int. J. Hydrogen Energy*, 2022, **47**, 40227–40241.
71 A. Tiwari, A. Goutam, S. Sk, P. Vijayanand, B. M. Abraham and U. Pal, *Int. J. Hydrogen Energy*, 2023, **48**, 29178–29188.
72 E. Pakizeh, M. Mohammadi and A. Mostafaei, *Solid State Commun.*, 2023, **369**, 115214.
73 M. Mohammadi and E. Pakizeh, *J. Electron. Mater.*, 2021, **50**, 4696–4704.
74 E. Pakizeh, *J. Mater. Sci.: Mater. Electron.*, 2020, **31**, 4872–4881.
75 E. Pakizeh, J. Jalilian and M. Mohammadi, *RSC Adv.*, 2019, **9**, 25900–25911.
76 C. Ni, C. Fu, B. Wang, H. Yuan and H. Chen, *Int. J. Hydrogen Energy*, 2021, **46**, 34305–34317.
77 W. Tang, G. Wang, C. Fu, B. Wang, H. Yuan and H. Chen, *Appl. Surf. Sci.*, 2023, **626**, 157247.
78 K. Ren, J. Yu and W. Tang, *J. Appl. Phys.*, 2019, **126**, 065701.
79 F. Rodríguez-Hernández, D. C. Tranca, A. Martínez-Mesa, L. Uranga-Piña and G. Seifert, *J. Phys. Chem. C.*, 2016, **120**, 25851–25860.